DE GRUYTER Nanotechnol Rev 2015; 4(2): 193–206

Review

Daniel M. Chevrier, Rui Yang, Amares Chatt and Peng Zhang*

Bonding properties of thiolate-protected gold nanoclusters and structural analogs from X-ray absorption spectroscopy

Abstract: Subnanometer, atomically precise thiolate-protected gold nanoclusters represent an important advancement in our understanding of thiolate-protected gold nanoparticles and thiolate-gold chemistry. Aside from being a link between larger gold nanoparticles and small gold complexes, gold nanoclusters exhibit extraordinary molecule-like optical, electronic, and physicochemical properties that are promising for next-generation imaging agents, sensing devices, or catalysts. The success in elucidating a number of unique thiolate-gold surface and gold core structures has greatly improved our understanding of thiolate-gold nanoclusters. Nevertheless, monitoring the structural and electronic behavior of thiolate-protected gold nanoclusters in a variety of media or environments is crucial for the next step in advancing this class of nanomaterials. Not to mention, there are a number of thiolate-protected gold nanoclusters with unknown structures or compositions that could reveal important insights on application-based properties such as luminescence or catalytic activity. This review summarizes some of the recent contributions from X-ray absorption spectroscopy (XAS) studies on the intriguing bonding properties of thiolate-protected gold nanoclusters and some structural analogs. Advantages from XAS include a local structural, site- and element-specific analysis, suitable for ultra-small particle sizes (1–2 nm), along with versatile experimental conditions.

Keywords: gold; nanoclusters; thiolate-gold; X-ray absorption spectroscopy.

DOI 10.1515/ntrev-2015-0007
Received February 4, 2015; accepted March 7, 2015; previously published online March 27, 2015

1 Introduction to gold nanoclusters

The chemical and optical properties of gold have captivated humankind for hundreds of years. Modern day research has focused on nanosized gold (e.g., gold nanoparticles) for applications in areas such as medicine and catalysis [1, 2]. Gold has robust chemical properties in bulk form and in nanosize form, making it a suitable element to study the synthesis and properties of nanostructured materials [3]. Remarkably, immense progress has been made in the last 20–30 years to attain a more intimate knowledge of gold nanoparticle structure-property relationships. The versatility of nanostructured gold has been demonstrated through the synthesis and fabrication of various 1-D, 2-D, and 3-D nanomaterial morphologies (e.g., nanowires, nanoprisms, and nanocubes) leading to size- and shape-specific properties [4, 5]. Nevertheless, there is still a persistent motivation to understand the origin of gold nanomaterial properties on a fundamental level. A new and prominent vein of research includes the study of quantum-sized or ultra-small gold nanoparticles, known as gold nanoclusters [6]. On this size regime, the electronic and bonding properties are more molecule-like in nature, leading to unexpected chemical and physical properties [7].

Gold nanoclusters (Au NCs) are composed of only 10s or 100s of Au atoms, which typically have a particle diameter of <2 nm. Au NCs are often synthesized with a monolayer of ligands on the surface that protect the Au core [8, 9]. Although Au NCs can be formed with weaker protecting ligands (e.g., biomolecules, dendrimers, polymers), this review will focus on highly stable, small ligand-protected Au NCs. Recent synthetic strategies adapted from the widely used two-phase Brust-Shiffiren [10] method have been successful in obtaining single-size thiolate-protected Au NCs (the chemical formula $[Au_n(SR)_m]^q$ is often used to describe the composition of single-sized Au NCs products; where n is number of Au atoms, m is the number of thiolate ligands (SR), and q is the total valence charge

---

***Corresponding author: Peng Zhang,** Department of Chemistry, Dalhousie University, Halifax, NS, Canada B3H 4R2; and School of Biomedical Engineering, Dalhousie University, Halifax, NS, Canada B3H 4R2, e-mail: peng.zhang@dal.ca
Daniel M. Chevrier, Rui Yang and Amares Chatt: Department of Chemistry, Dalhousie University, Halifax, NS, Canada B3H 4R2

on the cluster, if any) [11]. As a result of their small size, discrete valence electronic states are found for $Au_n(SR)_m$ instead of a quasi-continuous 5d band commonly seen for larger plasmonic Au NPs [6]. Therefore, electronic transitions exist between HOMO-LUMO levels, leading to the appearance of molecule-like properties (e.g., luminescence [12–14]). These unique properties are promising for widespread application in fields such as nanocatalysis [15] and bioimaging [16]. Interestingly, certain sizes of atomically precise Au NCs have been shown to follow a magic number series or superatom electronic shell-closing model providing a theoretical basis for their extraordinary stability [6, 8, 17, 18].

Despite the diverse range of protecting ligand types suitable for Au NC synthesis, thiolate ligands have demonstrated excellent stability and versatility in surface functionalization [17]. Since the elucidation of the $Au_{102}(SR)_{44}$ NC in 2007 [19], the catalog of possible Au core geometries and stabilizing surface structures from solved crystal structures and DFT predictions has grown significantly [20]. To date, icosahedral, face-centered-cubic (FCC)-ordered and smaller Au core (<13 Au atoms) structures have been reported crystallographically for various $Au_n(SR)_m$ sizes [19, 21–30]. A couple of selenolate-protected Au NCs have also been recently elucidated with icosahedral or small Au_8 core structures [31, 32]. In the last few years, a number of surface structures in addition to the monomeric and dimeric staple-like motifs were identified such as a trimeric staple-like motif [28], tetrameric staple-like motif [29, 30], μ^3 sulfide coordination [25], bridging thiolate motif [24], and ring-like motifs (long Au-SR oligomers) [27, 33]. Figure 1 presents the diversity of thiolate-protected Au NC structures. Currently, only the dimeric staple-like motif and ring-like motif have been confirmed to exist in structurally analogs selenolate-protected Au NCs [31, 32].

Uncovering the crystal structure of atomically precise Au NCs can provide important insights on the electronic structure, stability, and unique coordination environments of Au. Nevertheless, there is still plenty to uncover on the structural and electronic properties of Au NCs in response to chemical or physical processes such as ligand exchange, heteroatom metal doping, catalytic reactivity, and interactions/stability in complex biological systems. Intimate knowledge of these structure-property relationships could be vital in order for Au NC applications to come to fruition. Additionally, it is worthwhile to study Au NCs with well-defined core and surface structures in order to help predict the existence of such features in newly isolated Au NCs without an obtainable crystal structure. This significant obstacle originates from the inherently small nature of the Au NC size regime. The lack of a repeating gold lattice in Au NCs and the challenge of growing single crystals prevent or limit X-ray scattering and electron microscopy techniques from obtaining crystal packing information of the Au core. Additionally, the organoligand-Au interface is essentially undetectable with such techniques. A promising experimental approach in recent years has been to utilize X-ray absorption spectroscopy (XAS) to investigate the local structure of Au NCs from an element- and site-specific perspective.

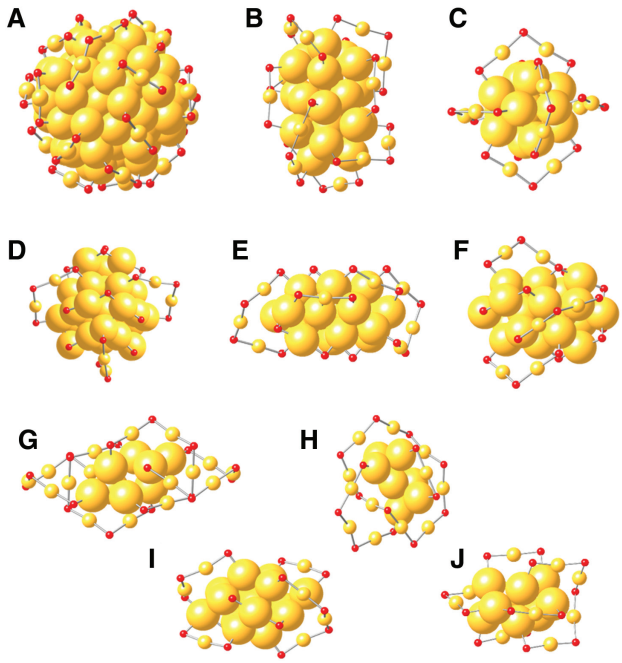

Figure 1: Elucidated $Au_n(SR)_m$ nanoclusters by X-ray crystallography (large yellow – core Au, small yellow – staple Au, red – S). Icosahedral-based: (A) $Au_{102}(SR)_{44}$, (B) $Au_{38}(SR)_{24}$, (C) $[Au_{25}(SR)_{18}]^{-,0}$, FCC based: (D) $Au_{36}(SR)_{24}$, (E) $Au_{30}S(SR)_{18}$, (F) $Au_{28}(SR)_{20}$, small or miscellaneous Au cores: (G) $Au_{24}(SR)_{20}$, (H) $[Au_{23}(SR)_{16}]^{-}$, (I) $Au_{20}(SR)_{16}$, and (J) $Au_{18}(SR)_{14}$. Carbon and hydrogen atoms are removed for clarity.

There are several advantages for using XAS including the measurement of subnanometer particle sizes (or seemingly amorphous materials), variable experimental conditions (solution-phase, temperature, *in situ* redox), multiple absorption edges for different elements (Au, S, Se, etc.) can be probed, and data analysis can reveal both metal-metal and metal-ligand structural environments. This review will summarize the capabilities of using XAS to study the structural and electronic properties of atomically precise, thiolate-protected Au NCs. Recently synthesized $Au_n(SR)_m$ NC structural analogs containing selenolate and tellurolate ligands will also be covered. A comprehensive review on some of our group's thiolate-protected Au NC research was recently published [34], where XAS and/or XPS studies on $Au_{144}(SR)_{60}$, $Au_{38}(SR)_{24}$,

$Au_{36}(SR)_{24}$, $Au_{25}(SR)_{18}$, $Au_{24}Pt(SR)_{18}$, and $Au_{19}(SR)_{13}$ NCs have been discussed. Before presenting some of the current XAS work in the community of thiolate-protected Au NC research, a brief description of the X-ray absorption process and data analysis is given first.

2 Introduction to X-ray absorption spectroscopy

XAS is inherently a local structure experimental technique commonly used to probe the coordination number and bond distance of the nearest atomic neighbors to the absorbing element. The X-ray absorption measurement is conducted in a relatively straightforward manner where modulation in the absorbing atom's X-ray absorption coefficient is measured and plotted as a function of incident X-ray energy. The first region of the XAS spectrum, known as X-ray absorption near-edge structure (XANES), is where the incident X-ray energy is increased from below the desired absorbing atom's core level (e.g., Au L_3-edge ($2p_{3/2}$) at 11,919 eV, known as the absorption edge energy (E_0)) to about 40–50 eV above. A few eV after the absorption edge energy, the first commonly observable feature is historically known as the white-line intensity. This transition occurs due to the promotion of excited core electrons to unoccupied valence levels via a dipole-allowed transition [35]. The white-line intensity can, therefore, be used quantitatively or qualitatively to determine the electronic structure of the valence level for the absorbing element. The intensity of the white-line feature is an average of all the absorbing elements in the measured sample, so it does not offer a site-specific perspective of the valence electronic structure. Near-edge features following the white-line can also be indicative of the absorbing atom coordination environment or geometrical orientation of nearest neighboring atoms and other available electronic transitions due to neighboring atoms. As the energy of the incident X-rays increases past the near-edge region of the spectrum, the excited core electrons will leave the absorbing atom in the form of a photoelectron wave. Emitted photoelectron waves will backscatter off electron shells of neighboring atoms with some photoelectron waves returning to the absorbing atom, quenching the core-hole excited state. Again, XAS is inherently a local structure technique as the emitted photoelectron wave will decay over time and distance due to inelastic losses. Therefore, interpretation of the nearest neighbors is largely limited to the first few scattering shells around the absorbing atom. As the energy is modulated, the photoelectron waves will experience constructive and deconstructive interference due to various backscattering paths. This will, in turn, influence the X-ray absorption coefficient of the element over the energy range measured creating the oscillatory part of the XAS spectrum known as the extended X-ray absorption fine structure (EXAFS) region. A rigorous mathematical treatment of the X-ray absorption process can be found in other works [35, 36].

Post-edge oscillations (often isolated as *k*-space spectra) can be further analyzed to determine the contribution of different scatterers to the overall EXAFS signal. The local scattering is typically represented in radial space (R-space) by applying a Fourier transform (FT) to a desired range of the *k*-space. This provides a qualitative view of the local structure environment around the absorbing atom without fitting the EXAFS data. Although it is possible to obtain structural details of the sample by fitting longer-range single scattering or multiple scattering features in the EXAFS spectrum [37], this can be difficult for Au NC samples due to the small particle size and short-range order. In this review, single scattering shells are mainly interpreted for various metal-ligand and metal-metal scattering paths. Modern EXAFS fitting methods use theoretical scattering paths generated from *ab initio* calculations to obtain backscattering amplitude functions and phase-shift values for different scattering environments in order to represent the major scattering shells in the EXAFS data [38, 39]. Using a theoretical scattering path to fit the EXAFS data, quantitative structural parameters can then be extracted from the EXAFS equation to provide the coordination number (CN), bond distance (R), and the Debye-Waller factor, a measure of static and thermal disorder ($\sigma^2=\sigma^2_{static}+\sigma^2_{thermal}$). One caveat of EXAFS fitting is the limited number of independent parameters available to work with. Meaning, not every unique scattering path can be incorporated into the fit as each scattering path will contain up to four free-running parameters (aforementioned CN, R, and σ^2, along with ΔE_0). In order to maximize the number of independent parameters, a long *k*-range can be selected for the FT to R-space given that the late *k*-space oscillations are distinct and not overruled by experimental noise. As an aside, if a multi-shell EXAFS analysis is to be conducted on a Au NC sample, where weaker and long distance single scattering paths are used to fit the data (e.g., aurophilic interactions), the XAS experiment should be conducted at low temperature (~77 K) and with a large beam spot on the sample to enhance the late *k*-space oscillations and avoid beam damage, ensuring the EXAFS data is reproducible. A wide R-space fitting window can also be used to increase the number of independent parameters. However, it is recommended that the number of free-running parameters should be less than the total number of independent parameters, if not around half of the number of independent parameters.

There are two general approaches that can be applied to fit the EXAFS of Au$_n$(SR)$_m$ NCs and other metal NC systems. Au L$_3$-edge EXAFS will be focused on, which is more commonly probed. If the total structure of the Au NC has not been solved crystallographically, the number of scattering shells used to fit the data will be limited. It is difficult to reliably determine what range of bonding types the scattering shell will encompass (center to surface and/or surface to surface) without knowledge of the core or surface structure. Thus, two scattering shells, Au-ligand and Au-Au core interactions, can be incorporated confidently without contribution from longer Au-ligand, longer Au-Au, or multiple scattering paths. The EXAFS-determined CN values for each scattering shell provide structural information on the size and relative thiolate:Au ratio. If the Au$_n$(SR)$_m$ NC composition is known from mass spectrometry (MS) measurements, CN and R values for each shell can be used to help infer more local structural details. The second EXAFS fitting method expands on the interpretation of Au$_n$(SR)$_m$ NC local structure by using an available total structure model to identify distinct scattering paths that account for core, surface, and possibly aurophilic interactions (two to three Au-Au scattering shells total). Scattering shells can be assigned confidently if there is a clear separation in bond distance for each scattering environment. For example, Au$_{25}$(SR)$_{18}$ NCs have Au-Au interactions on the surface around 2.95 Å and between surface and staple sites around 3.16 Å. The bond length distribution for each shell is completely separated to ensure little overlap of different scattering environments. The EXAFS-determined R values for each shell should then be compared with the crystal structure model to ensure the correct site-specific representation of each distinct scattering path. This second fitting method allows interpretation of Au$_n$(SR)$_m$ NC EXAFS data from a site-specific perspective. With a highly pure sample and known structural framework, CN values can be calculated and fixed in the EXAFS fitting analysis to lower the number of free-running parameters. ΔE_0 parameters for similar scattering paths can also be correlated to minimize the number of free-running parameters, if needed. This multi-shell fitting methodology was proven to be effective for detecting the structural response of Au$_{25}$(SR)$_{18}$ NCs to solvent and temperature by monitoring changes in bond length and disorder [40]. See Figure 2 for a simulated Au L$_3$-edge EXAFS spectrum, indicating each distinct scattering shell that can be interpreted in the EXAFS spectrum of Au$_{25}$(SR)$_{18}$ NCs. Au-Au CN values are also extremely sensitive to a small change in Au NC composition given their subnanometer size [41]. As the EXAFS signal is averaged over all absorbing atoms, larger Au NPs will not see such a dramatic change in Au-Au coordination with a small change in composition due to the higher amount of atoms in the core versus on the surface. A comprehensive review on the geometrical and compositional characterization of NPs from EXAFS can be found by Frenkel et al. [42].

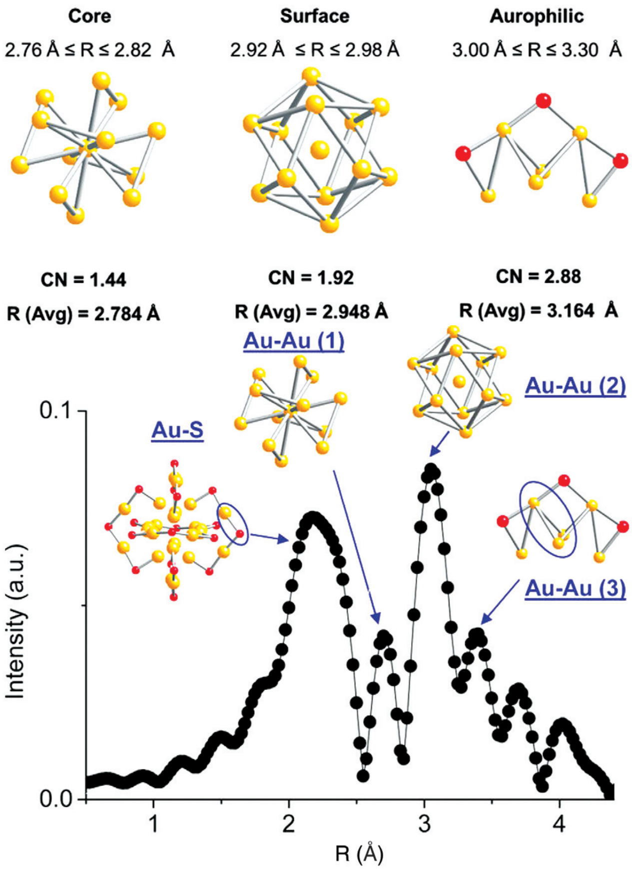

Figure 2: Distinct Au-Au bonding environments of the Au$_{25}$(SR)$_{18}$ NC (top) and simulated EXAFS spectrum for Au$_{25}$(SR)$_{18}$ (phase-corrected) with scattering features identified for each site-specific bonding type (bottom). Reproduced with permission from Ref. [40].

3 Thiolate-protected gold nanoclusters

Atomically precise phosphine- and halide-protected Au NCs first sparked an interest in many researchers for studying the composition-dependent properties of Au

NPs. The famous Schmid cluster, $Au_{55}(PPh_3)_{12}Cl_6$ [43] was one of the first size-specific Au NCs studied with XAS in the 1990s [44–46]. Au L_3-edge EXAFS fitting results from a few studies suggested the Au core is likely cuboctahedral instead of icosahedral. Further analysis of the $Au_{55}(PPh_3)_{12}Cl_6$ with EXAFS by Cluskey et al. suggested a possible arrangement of phosphine and chloride ligands on the surface [44]. Marcus et al. probed the thermal vibrational properties using temperature-dependent XAS measurements [46]. This early use of XAS to study Au_{55} proved to be a beneficial approach for investigating the structure and properties of ultra-small Au NCs. Nevertheless, the synthesis of thiolate-protected gold nanoparticles had made exceptional progress through the late 1990s and early 2000s with the Brust-Schiffrin synthetic procedure [10]. This breakthrough led to the successful synthesis and crystallization of two highly stable, thiolate-protected Au NCs, $Au_{102}(SR)_{44}$ and $Au_{25}(SR)_{18}$, reported in 2007 and 2008, respectively [19, 22, 23]. Attention had then shifted to the exciting revelation of icosahedral core structures and staple-like Au-SR oligomer motifs on the surface (shown in Figure 1).

$Au_n(SR)_m$ NCs are being recognized as promising catalysts for a variety of oxidation/reduction reactions [15, 47, 48]. For larger metal NP catalysts, XAS characterization has been utilized to detect changes in surface local structure after catalytic treatments [49, 50]. Such structural information is crucial for identifying and further understanding the catalytically active locations on the surface of the metal NP or NC. A study by Shivhare et al. demonstrated that partially or completely removing the protecting ligands from alkanethiolate-protected Au_{25} NCs (supported on carbon powder) by calcination increased the catalytic reduction of 4-nitrophenol [51]. Au L_3-edge EXAFS spectra for $Au_{25}(SC_8H_9)_{18}$ and $Au_{25}(SC_6H_{13})_{18}$ were collected before thermal treatment and fitted using four shells to confirm the core and surface local structure of the NC samples. Results were consistent with a previous EXAFS study on $Au_{25}(SC_8H_9)_{18}$ [40]. TEM was used in conjunction with Au L_3-edge EXAFS measurements (temperature-dependent EXAFS spectra are depicted in Figure 3) to monitor particle growth with thermal treatment. It was found from EXAFS fitting results that Au_{25} NCs undergo partial cluster sintering at a mild calcination temperature of 150°C where the Au-S CN decreased, and the core Au-Au bond length increased to 2.85 Å from 2.76–2.80 Å at room temperature. At higher temperatures of 200°C the Au-Au CN increased to nine and the Au-S CN decreased to 0.6–0.8, for both thiolate-protected Au_{25} NCs. The small increase in Au NC particle size and EXAFS fitting results suggest there was partial removal of surface thiolate ligands and small Au core growth around 200°C. It is around this temperature that Au_{25} NCs showed the highest rate constant for the reduction of 4-nitrophenol. This finding supports the hypothesis that the Au core surface is an important location for catalytic activity. It was also evident by qualitative comparison of the two thiolate-Au_{25} systems in Figure 3 that phenylethanethiolate ligands are thermally removed before hexanethiolate ligands, indicating the type of thiolate ligand could impact the catalytic activity of thermally treated $Au_n(SR)_m$ NCs. A similar study by Liu et al. compared the activity of $[Au_{25}(PPh_3)_{10}(SC_{12}H_{25})_5Cl_2]^{2+}$ and $[Au_{25}(SC_8H_9)_{18}]^-$ ($Au_{25}(SR)_{18}$ before and after calcination on a SiO_2 support [52]. Au L_3-edge EXAFS results for $Au_{25}(SR)_{18}$ on SiO_2 indicated the thiolate ligands were mostly removed by 200°C in air and by 300°C under He gas. From their analysis of the Au-Au EXAFS fitting results, they suggested that the Au core grew after the removal of thiolate ligands with the Au-Au bond distance remaining around 2.82–2.84 Å, while remaining

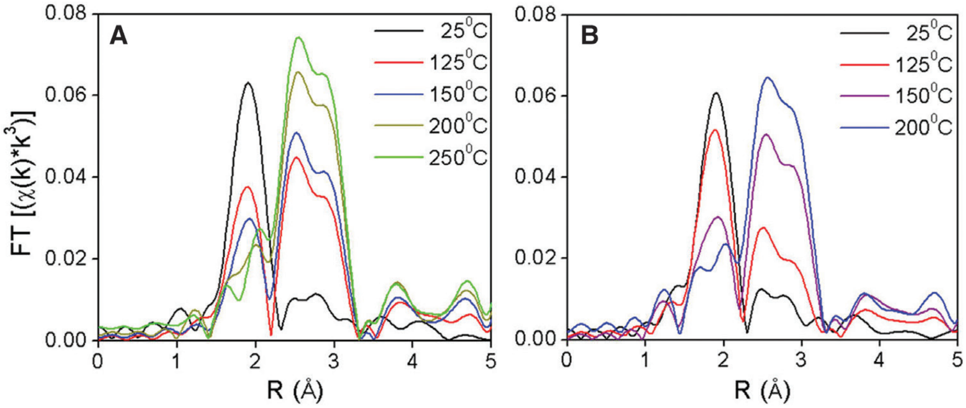

Figure 3: Temperature-dependent Au L_3-edge EXAFS of phenylethanethiolate-Au_{25} (A) and hexanethiolate-Au_{25} (B) NCs supported by carbon powder. Reprinted with permission from Ref. [51].

much shorter than bulk Au (2.88 Å). After performing the styrene oxidation reaction with $Au_{25}(SR)_{18}$, the Au-Au CN was found to decrease only slightly from 9.5 to 8.5. Monitoring the structure of $Au_n(SR)_m$ NCs *in situ* catalysis reaction or post-catalytic treatment with EXAFS should be considered in future work in this area as the local structure and element-specific perspective from XAS can be used to help detect small changes on the Au NC surface or in the core.

An alkanethiol ligand-exchange-induced formation of $Au_{38}(SR)_{24}$ NCs from polydisperse $Au_n(SG)_m$ NCs (SG – glutathione) was reported by Stellwagen et al. [53]. The authors used FT-IR to confirm that all tested alkanethiol molecules over various lengths were bound to the Au NC; moreover, in an all-*trans* configuration. Au L_3- and S K-edge XANES results (shown in Figure 4) were used to further demonstrate that all lengths of tested alkanethiol ligands were completely ligand exchanged. From the Au L_3-edge XANES, mainly the white-line feature can be interpreted to deduce the occupation of 5d electronic states, but for S K-edge, the near-edge region is sensitive to more changes in the structural and electronic environment, which can be observed through the E_0 shift, white-line intensity, and post- and pre-edge features. Formation of S-metal bonds produces a noticeable change in the near-edge region due to the appearance of vacant electronic states from the metal atom. For example, quadrupole transitions from orbital mixing of S 1s and the vacancies in the *n*d level of the bonded metal atom (e.g., 5d from Au) can be observed as pre-edge features in S K-edge XANES [54]. All thiolate-protected Au_{38} NCs showed a broadening of the white-line feature from the pure thiol reference due to the formation of S-Au interactions but were all still narrower than the white-line feature for Au_2S reference, indicating the more molecule-like Au(I)-SR interactions in staple-like motif structures. Therefore, the first S K-edge XANES feature can serve as a quick indication of a thiolate or sulfide environment. Anomalously, all alkanethiolate-protected Au_{38} NCs except for hexanethiolate-protected Au_{38} exhibited a pre-edge shoulder. This anomaly could be related to impurities, which the authors pointed out with discussion of weak UV-Vis absorption features. This pre-edge feature for S K-edge has been shown to be size dependent in other work and likely related to the size of the Au core [55], but was not further inspected in this work by Stellwagen et al. Overall, S K-edge near-edge features and the relative white-line intensity from Au L_3-edge XANES supported the presence of staple-like Au-SR motifs and charge transfer from Au to S for varied lengths of alkanethiolate-protected Au_{38} NCs.

On the topic of Au-SR surface interactions, Au L_3-edge EXAFS was employed by Tsukuda et al. to investigate a unique binding motif for sterically demanding thiolates for $Au_{41}(S\text{-}Eind)_{12}$ (S-Eind-1,1,3,3,5,5,7,7-octaethyl-*s*-hydrindacene-4-thiol) [56]. The total structure of $Au_{41}(S\text{-}Eind)_{12}$ was not elucidated in this work or in previous work. Thus, only a two-shell EXAFS fit was conducted to probe the relative Au core size and the amount of thiolate-Au bonding. A high Au-Au CN was found from EXAFS fitting of $Au_{41}(S\text{-}Eind)_{12}$ (4.1±0.4), which is much higher than $Au_{38}(SC_{18}H_{37})_{24}$ (1.7±0.2) and, in fact, more comparable to $Au_{\sim 43}$ NCs (4.4±0.4) stabilized by weakly

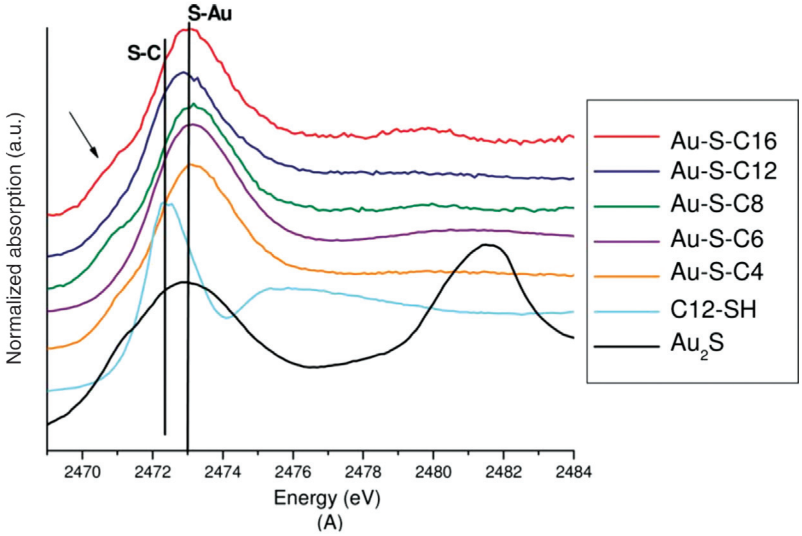

Figure 4: S K-edge XANES spectra of *n*-alkanethiolate-Au_{38} NCs after thiol-etching of polydisperse $Au_n(SG)_m$ NCs. Reproduced with permission from Ref. [53].

coordinating polyvinylpyrrolidone (PVP). A comparison of each R-space spectrum is shown in Figure 5. This EXAFS fitting result of the main Au-Au scattering shell suggested most of the Au atoms are consolidated in the Au core with few, if any, Au atoms held away from the Au core in Au-SR oligomer-protecting structures (i.e., staple-like motifs). A μ^3-like bonding motif was proposed, considering the average CN for the Au-S scattering shell (0.9±0.4) and composition of $Au_{41}(S\text{-}Eind)_{12}$, where each sterically demanding S-Eind ligand is bonded to three Au surface atoms on average. It should be noted that a μ^3-like bonding motif was recently elucidated on the $Au_{30}S(SR)_{18}$ NC, where only one sulfur atom interacts with the Au NC surface, but as a sulfide instead of a thiolate [25]. Finally, although each Au NC measured in this work has a similar number of Au atoms (Au_{38}, Au_{41}, and $Au_{\sim 43}$), it is clear that the amount of ligand-Au interactions dramatically affects the scattering peak intensities in the EXAFS spectrum, as demonstrated in Figure 5.

A recent study on the identification of a highly luminescent $Au_{22}(SG)_{18}$ NC (SG – glutathione) was reported by Yu et al. [57]. The strong luminescence property was thought to originate from longer Au-SR oligomeric motifs on the NC surface based on previous studies of aggregation-induced emission [58]. Au L_3-edge XAS analysis was used to help predict the structural environment of $Au_{22}(SG)_{18}$ in combination with a proposed DFT-optimized model. Of the generated DFT-optimized structures, a $Au_{22}(SR)_{18}$ NC with one RS-$[Au\text{-}SR]_3$ and one RS-$[Au\text{-}SR]_4$ motif were predicted to interlock with each other on each end of a prolate Au_8 core (four Au-SR oligomeric structures total). EXAFS-determined CN values from the Au-S scattering shell and the shortest Au-Au scattering shell were consistent with the proposed model within the reported fitting uncertainties. The average Au-Au bond length in the predicted Au_8 core was found to be 2.67(1) Å, which is significantly shorter than Au-Au bonding in most known Au core structures. Together, MS and DFT/EXAFS characterization provided convincing evidence for a Au_8 core with interlocking Au-SR oligomers as the strongly luminescent Au(SR) NC product.

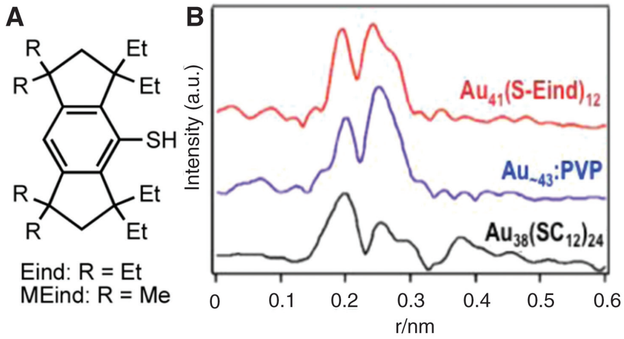

Figure 5: Sterically demanding thiol ligand (A) used to protect $Au_{41}(SR)_{12}$ NCs. Au L_3-edge EXAFS comparison (B) of similar size Au NCs but with varying ligand-Au interfaces. Reproduced with permission from Ref. [56].

A more recent study on the bonding properties of $Au_{28}(SR)_{20}$ NCs from XAS was reported by our research group. Temperature-dependent bonding properties of $Au_{28}(SR)_{20}$ were examined by fitting Au L_3-edge EXAFS data measured at 90 and 300 K. At both measured temperatures, short Au-Au interactions related to Au_4 core structures remain around 2.74 Å in distance. A second, longer Au-Au scattering shell representing Au-Au interactions between tightly bonded Au4 units and on the surface of the Au core fitted in the EXAFS spectra appeared to contract at the 300 K (from 2.99 (3) to 2.93 (3) Å). A similar thermal contraction property was observed for the larger FCC-ordered relative, $Au_{36}(SR)_{24}$. $Au_{28}(SR)_{20}$ NCs were found to have a highly occupied 5d electron valence state compared with similar-sized $Au_{25}(SR)_{18}$, consistent with the previous XAS study on $Au_{36}(SR)_{24}$ when compared to similar-sized icosahedral-based $Au_{38}(SR)_{24}$ [59]. This XAS work on FCC-ordered $Au_n(SR)_m$ NCs communicates the apparent influence of smaller Au_4 core structures on the electronic and temperature-dependent bonding properties of FCC-ordered $Au_n(SR)_m$ NCs. It is anticipated that XAS elucidation of these unique structural and electronic characteristics could be used to distinguish FCC-ordered Au NCs from icosahedral-based Au NCs when the total structure is unknown. Importantly, this should be tested with additional FCC-ordered Au NCs to confirm the potentially identifiable characteristics of Au_4 units.

3.1 Metal dopants in thiolate-protected Au NCs

Correlating the structural and electronic properties of Au NCs with their catalytic activity and optoelectronic characteristics is undoubtedly an important step forward in preparing atomically precise Au NCs for application purposes. In addition to modifying the ligand, surface structure or size, an interesting area in Au(SR) NC research is tuning the electronic properties by introducing a metal dopant, usually noble or late transition metals. Although a number of heteroatoms can be added to the Au NC composition, identifying the most thermodynamically favorable site in Au NCs for a single heteroatom is an intriguing and important question from the nanochemists' perspective. Few heteroatom-doped Au NCs also represent some of the smallest nanoalloys synthetically possible [60, 61]. With only a few crystal structures of heteroatom-doped Au NCs presently known [62], the preferred location of the metal dopant and its effect on the Au NC structure can be investigated through XAS measurements. Conveniently, XAS experiments can probe both the Au L_3-edge and the L_3- or K-edge of a 3d, 4d, or 5d heteroatom to provide complimentary data, pinpointing the location of the dopant site (center, surface, or staple). Here, a few studies on heteroatom-doped thiolate-protected Au_{25} are summarized.

The dopant location and electronic properties of monopalladium-doped Au_{25} NCs ($Au_{24}Pd(SR)_{18}$) were investigated with Pd K-edge XAS, using [197] Au Mossbauer spectroscopy for complementary data of the Au local structure [63]. By comparing the Pd K-edge EXAFS oscillation pattern of the sample with the theoretical pattern of each dopant location scenario (Pd in the center, surface, or staple, as seen in Figure 6) and fitting the EXAFS data, it was clear that Pd was located in the center position with a high Pd-Au CN of 10.7. Consistent with the $Au_{24}Pt(SR)_{18}$ sample studied by Christensen et al. [65], both d^9 metals caused a small contraction of the icosahedral core where the center M-Au bond length averages ~2.75 Å. XANES spectra at both absorption edges were used to deduce intracluster charge transfer from the central Pd site to surrounding Au by observing a decrease in Au L_3 white-line intensity and a positive shift in Pd K-edge E_0 position relative to bulk Pd. In the latter experimental observation, a small shift of the core electron-binding energy (shown by plotting the first derivative of Pd foil, $Au_{24}Pd$, and Na_2PdCl_4) to higher-energy supports valence electrons are transferred to neighboring Au atoms.

Au_{25} NCs doped with Cu or Ag atoms were most recently studied using XAS in conjunction with DFT calculations [64]. $Au_{23.8}Ag_{1.2}(SR)_{18}$ and $Au_{23.6}Cu_{1.4}(SR)_{18}$ NCs were synthesized (protected by phenylethanethiol), having compositions very close to single atom-doped Au_{25} NCs. First, DFT-optimized structures were determined for each system ($Au_{24}M(SR)_{18}$, where M is Ag or Cu) and for each possible dopant site location (center, surface, and staple). From these models, Ag K-edge and Cu K-edge EXAFS spectra were simulated to compare with experimental data using a R^2 factor method to determine the agreement between simulated and experimental EXAFS. For the monosilver system, EXAFS fitting results and comparison to simulated EXAFS of a Ag surface site dopant site for Au_{25} suggested Ag prefers the surface of Au_{25} from agreeable Ag-Au and Ag-S CN values. The EXAFS-determined Ag-S bond length increases to 2.443 Å, consistent with an increase from the DFT model. For the monocopper system, both EXAFS and XANES results (shown in Figure 6) from the Cu K-edge perspective show the Cu atom occupies the staple site in Au_{25} NCs instead of the surface or core. Convincingly, only Cu-S bonding around 2.2 Å was evident

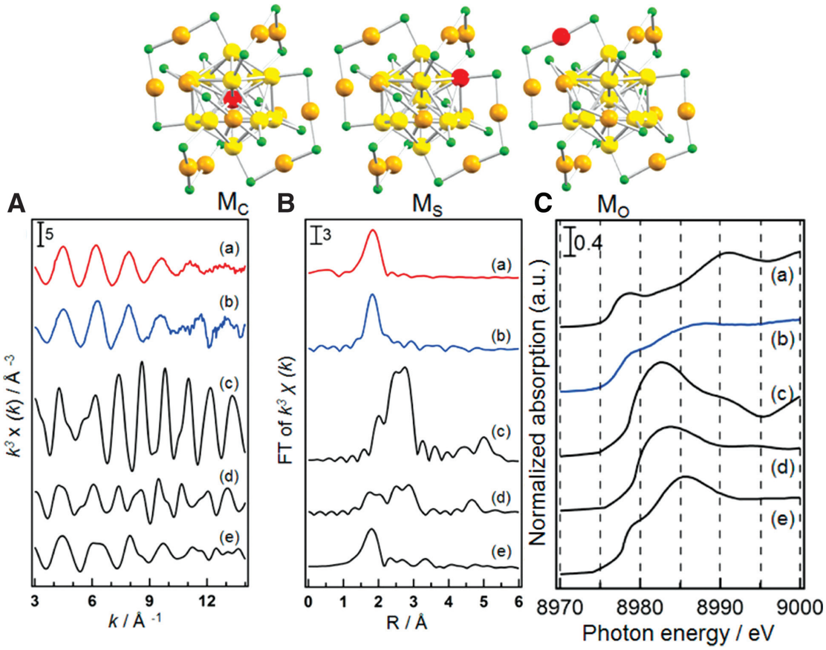

Figure 6: Possible metal dopant locations in $Au_{25}(SR)_{18}$ NCs (top). Cu K-edge k-space (A), FT-EXAFS (B) and XANES (C). Experimental data for $Au_{23.6}Cu_{1.4}(SR)_{18}$ at (a) 300 K and (b) 8 K along with simulated spectra for (c) center, (d) surface, and (e) staple dopant sites. (XANES spectrum (a) is from Cu foil.) Reproduced with permission from Ref. [64].

from the fit of the FT-EXAFS spectrum. As can be seen from these summarized $Au_{24}M(SR)_{18}$ studies, XAS is an invaluable characterization technique for determining the favorable location of various metals and could be extended to other metal-based NC systems besides Au_{25}. Moreover, this latter study exemplifies the useful collaboration of DFT structural optimization, XAS simulation, and experimental XAS studies to elucidate the prominent metal dopant site in Au(SR) NCs.

3.2 Selenolate- and tellurolate-protected analogs

Some studies have suggested that a heavier chalcogen head group (e.g., Se) could improve the stability of ligand-protected Au NCs and NPs [66, 67]. The isolation and structural characterization of dodecaneselenolate-protected Au_{38} clusters ($Au_{38}(SeC_{12}H_{25})_{24}$) was reported first by Kurashige et al. [68]. In this work, the local structure of $Au_{38}(SeR)_{24}$ was mainly characterized by Au L_3-edge EXAFS, as shown in Figure 7. $Au_{38}(SC_{12}H_{25})_{24}$ and Au foil were used to compare with selenolate-protected Au_{38} NCs. The scattering shell for Au-Se was shifted by about 0.1 Å (fitted Au-Se bond distance of 2.43 Å) and much broader compared to a Au-S scattering shell from $Au_{38}(SC_{12}H_{25})_{24}$, likely due to the larger atomic radius of Se. Despite the overlap in Au-Se and Au-Au scattering, fitting the Au-Au scattering shell indicated a Au-Au core distance of 2.77 Å and average CN value similar to thiolate-protected Au_{38}, indicating a similar structural framework to well-defined $Au_{38}(SR)_{24}$ NCs. $Au_{25}(SeC_{12}H_{25})_{18}$ NCs were also measured with XAS in this work showing a shifted, broader Au-Se scattering shell with comparable EXAFS fitting results to $Au_{25}(SR)_{18}$. EXAFS results from both NC sizes infer the Au core structure in each selenolate-protected Au NC does not significantly expand, contract, or change composition. Nevertheless, additional Au-Au scattering shells were not used to inspect the surface and aurophilic interactions of selenolate-protected Au_{25} and Au_{38}. Interestingly, the white-line intensities of selenolate-protected Au_{38} and Au_{25} were, in fact, very near the intensity of bulk Au (as shown in Figure 7) indicating selenolate ligands dramatically affect the 5d valence electronic structure of Au, which may help account for enhanced stability of the Au NC.

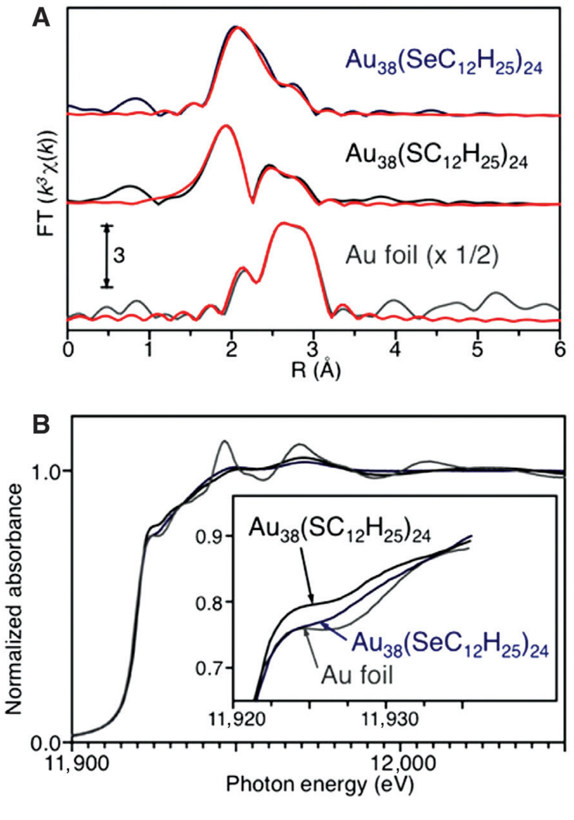

Figure 7: Au L_3-edge EXAFS and XANES of $Au_{38}(SeR)_{24}$ with $Au_{38}(SR)_{24}$ and Au foil for reference. Reproduced with permission from Ref. [68].

Intriguing bonding behavior of benzeneselenolate-protected Au_{25} NCs ($Au_{25}(SeR)_{18}$) was reported by our research group [69]. Au L_3-edge and Se K-edge XAS results were used to investigate the local structure and temperature-dependent bonding properties of $Au_{25}(SeR)_{18}$ NCs with the XAS data collected presented in Figure 8. Similar to the dodecanceselenolate-Au_{25} and -Au_{38} studied by Kurashige et al. [68], Au-Se bonding produced a broad scattering feature that partially overlapped with Au-Au scattering. Comparing EXAFS oscillations in the *k*-space at 50 K (Figure 8, top left), late *k*-space (8–13 $Å^{-1}$) oscillations were significantly more intense for the selenolate-protected Au_{25}, potentially from more tightly ordered Au-Au bonding. An understanding of the Au local structure was extended in this work by employing a four-shell EXAFS fit following a previously established fitting approach for $Au_{25}(SR)_{18}$ NCs [40]. At 50 K, Au-Se and core Au-Au bond distances from EXAFS fitting were consistent with Kurashige et al. [68]. The second Au-Au scattering shell indicated that the Au-Au interactions on the surface of the Au_{13} core were comparable to the thiolate-protected Au_{25}. However, fitting the third Au-Au scattering shell (from staple Au to surface Au) gave a long Au-Au distance suggesting substantially weaker aurophilic interactions compared with $Au_{25}(SR)_{18}$. When $Au_{25}(SeR)_{18}$ NCs were measured at 300 K, all three site-specific Au-Au bonding environments show a thermal contraction, while Se-C bonding appeared to expand with increasing temperature (Se K-edge EXAFS) (Figure 8 bottom right).

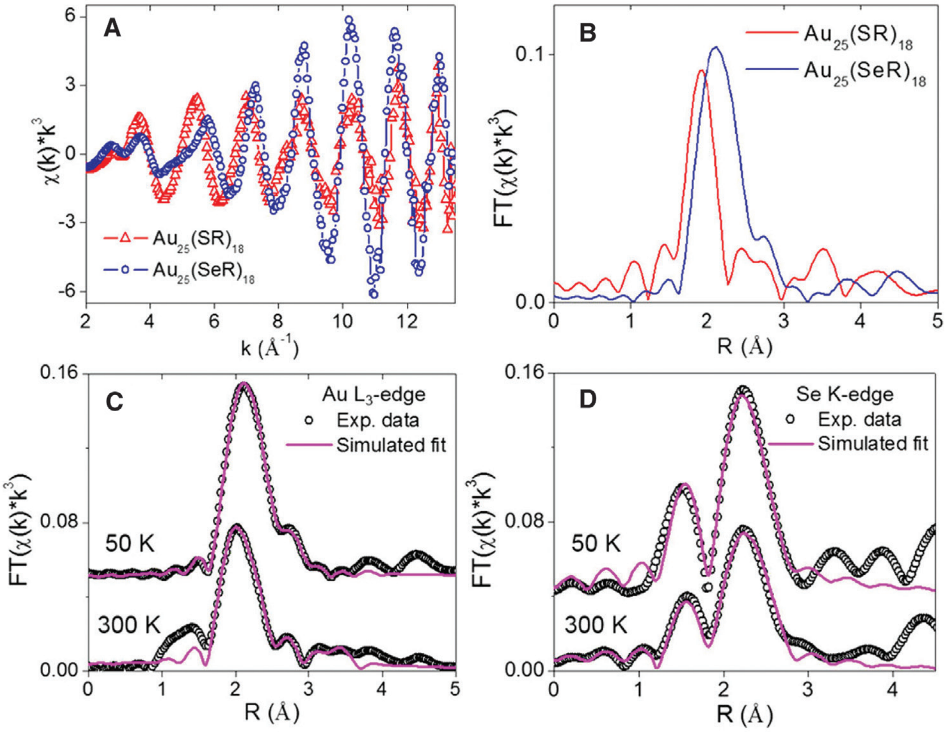

Figure 8: Au L_3-edge EXAFS in (A) *k*-space and (B) R-space for $Au_{25}(SeR)_{18}$ and $Au_{25}(SR)_{18}$. Temperature-dependent (C) Au L_3-edge and (D) Se K-edge EXAFS for $Au_{25}(SeR)_{18}$. Reproduced with permission from Ref. [69].

Unexpected temperature-dependent trends of the Debye-Waller factors for each Au-Au shell were also noted. Molecular dynamics simulation of the $Au_{25}(SePh)_{18}$ cluster at 300 K showed staple Au is drawn closer to the core by a conformational change in the dimeric staple structure, providing a potential mechanism of thermal contraction. For the electronic properties, the white-line intensity for $Au_{25}(SePh)_{18}$ at the Au L_3-edge was surprisingly even lower than bulk Au. From the Se K-edge perspective, an increase in the white-line intensity and small positive shift of the E_0 energy demonstrates the electron transfer from 4p when bonding with Au. As few studies have investigated the Se K-edge XANES for Au NCs, *ab initio* simulations of the near-edge region and density of states for Au, Se, and C sites were conducted to identify the origin of near-edge transitions. Important near-edge features include contributions from Se p-DOS, Se d-DOS, and C p-DOS from the organoselenolate ligand.

Thus far, only one XAS study has been conducted on tellurolate-protected Au NCs. Kurashige et al. demonstrated that benzenetellurol (HTePh) could be partially exchanged onto $Au_{25}(SR)_{18}$ forming various mixed ligand products of $[Au_{25}(TePh)_m(SR)_{18-m}]^-$ where m=~1, ~3, and ~7 [70]. Unique to tellurolate-protected Au NCs, no sign of oxidized telluride was found from Te K-edge XAS results, whereas oxides have been detected on larger tellurolate-protected Au NPs. From various EXAFS fitting approaches (two- and three-shell fitting), Au-Te bonds were found to exist around 2.58–2.59 Å in distance. By including one Au-Au scattering shell to account for shorter Au-Au interactions in the Au_{13} core, EXAFS fitting results indicated the Au-Au distance and coordination to be similar to pure thiolate-protected Au_{25} crystal structure and only slightly lengthened compared to the measured $Au_{25}(SR)_{18}$ reference. Selenolate- and tellurolate-protected Au NCs are excellent materials for XAS characterization as high-quality EXAFS oscillations can be collected at Se K- and Te K-edges, gaining or confirming the local structure of the Au-ligand interface.

4 Outlook and summary

It is anticipated that the use of XAS for the study of Au NC structural and electronic properties will continue to increase in popularity. It is challenging to predict the core and surface structure of Au NCs and to interpret the electronic properties with XAS measurements alone. As seen from the reviewed studies, having the support of MS, DFT *ab initio* simulations and/or single crystal X-ray structure, can provide the researcher with a basis to test the EXAFS fitting with various structural models. Mass spectrometry results can help account for the fitted CN values, based on the determined composition. With DFT-predicted structural models and *ab initio* XAS simulations, distinct scattering paths can be identified and utilized for EXAFS fitting purposes. The combination of MS, DFT, and EXAFS can be powerful when predicting the structure of the studied $Au_n(SR)_m$ NCs, but should be conducted with caution if there is no clear favorable structural isomer from DFT calculation. Unfixed Au-S or Au-ligand CN values from the EXAFS fit are a good first indication of the similarities between the data and the predicted model. In any case, the crystallographic total structure of a $Au_n(SR)_m$ NC is the most useful piece of information that can be used to explore the capabilities of EXAFS fitting. Importantly, if two scattering shells with the same absorbing and backscattering atoms are used to fit the experimental EXAFS data, the researcher should provide a means to clearly explain the scattering environment for each path used to fit the EXAFS. With confident assignment of each scattering path and enough representative scattering paths to account for the core and surface structure, the study of $Au_n(SR)_m$ NC bonding properties can be significantly enriched, allowing further exploration of the $Au_n(SR)_m$ NC structural response to a number of experimental conditions available at synchrotron beamline facilities.

EXAFS fitting methodologies and XAS experiments developed from studies on $Au_n(SR)_m$ NCs can easily be extended to other metal-based NC systems. Therefore, there will be a strong need for unifying or creating a standard fitting procedure for the study of NC systems so that results can easily be compared across various reports. Careful and well-designed XAS experimentation will hopefully lead to an improved understanding of important mechanisms concerning Au NC formation, solvent-cluster interactions, ligand exchange, and interactions with biological systems. These fundamental questions that have surrounded $Au_n(SR)_m$ NCs for many years could be answered in full, or in part, with XAS experimentation or characterization. Select studies on Au NCs that utilize the versatility of the experimental conditions or the *in situ* capabilities of an XAS experimental setup are briefly discussed below.

The role of the solvent type on the structure of Au NCs and smaller Au NPs has been studied recently with XAS [71, 72]. Through EXAFS analyses of Au NCs or Au NPs in various solvent conditions, such works have been able to identify solvent-induced transformations of the Au core structure or the thiolate surface coverage. On the formation of Au NCs and NPs, *in situ* or quick-XAS experiments are promising for observing the nucleation and subsequent directed growth of Au particles. Monitoring the reduction of Au^{3+} in the presence of thiol molecules via Au L_3-edge XANES and EXAFS by Ohyama et al. has shown evidence of Au_4 clusters in the early stages of nucleation [73]. Using the weaker protecting ligand PVP, Yao et al. observed the formation of Au_nCl_{n+x} complexes in the initial nucleation stage of Au NCs or Au NPs [74]. Further interpretation of their *in situ* EXAFS data leads to kinetic insights on three different stages of Au NC formation. Another step forward in EXAFS characterization of Au NC surface structure or the thiolate-Au interface is possible by combining DFT-molecular dynamics simulations and *ab initio* calculation of EXAFS spectra. Yancey et al. took this experimental-theoretical approach to study the surface structural disorder of $Au_{\sim 147}$ clusters protected by dendrimer molecules with increasing amounts of terminal thiols (12, 24, 50, and 72 thiols per $Au_{\sim 147}$ cluster) [75]. Remarkable similarities were reported for each $Au_{\sim 147}$ cluster with varied thiolate-Au interactions. This approach opens up new opportunities to more carefully interpret experimental EXAFS data for Au NCs with unknown surface and core structures. Finally, advanced XAS-related techniques such as X-ray excited optical luminescence [76] and high-energy resolved fluorescence detection [77] may offer new insights into the element-specific luminescence and time-resolved high-resolution valence electronic structure of Au(SR) NCs, respectively. Both techniques are employed when the absorbing atom's near-edge region is probed and can be compared with the conventional XANES.

In summary, XAS can serve as an excellent characterization technique to study the local structure and electronic properties of Au NCs from a site- and element-specific perspective. EXAFS is particularly useful for smaller Au NC systems (# of Au atoms<~50) as more distinct scattering shells can be resolved in the data without a strong contribution from the bulk of a large metal core. This review has demonstrated the utility of using XAS for investigating $Au_n(SR)_m$ NCs in catalysis, thiolate-Au surface bonding motifs, unknown $Au_n(SR)_m$ structures, temperature-dependent bonding properties, metal dopant location, and local structural/electronic properties of selenolate- and tellurolate-protected Au NCs.

Acknowledgments: PZ would like to thank the Natural Sciences and Engineering Research Council (NSERC) of Canada for financial support in the form of Discovery Grants, and DMC would like to thank NSERC for financial support through the Alexander Graham Bell Canada Graduate Scholarship.

References

[1] Hutchings GJ, Brust M, Schmidbaur H. Gold–an introductory perspective. *Chem. Soc. Rev.* 2008, 37, 1759–1765.

[2] Saha K, Agasti SS, Kim C, Li X, Rotello VM. Gold nanoparticles in chemical and biological sensing. *Chem. Rev.* 2012, 112, 2739–2779.

[3] Jain PK, Huang X, El-Sayed IH, El-Sayed MA. Noble metals on the nanoscale: optical and photothermal properties and some applications in imaging, sensing, biology, and medicine. *Acc. Chem. Res.* 2008, 41, 1578–1586.

[4] Daniel M-C, Astruc D. Gold nanoparticles: assembly, supramolecular chemistry, quantum-size-related properties, and applications toward biology, catalysis, and nanotechnology. *Chem. Rev.* 2004, 104, 293–346.

[5] Grzelczak M, Pérez-Juste J, Mulvaney P, Liz-Marzán LM. Shape control in gold nanoparticle synthesis. *Chem. Soc. Rev.* 2008, 37, 1783–1791.

[6] Jin R. Quantum sized, thiolate-protected gold nanoclusters. *Nanoscale* 2010, 2, 343–362.

[7] Wilcoxon JP, Abrams BL. Synthesis, structure and properties of metal nanoclusters. *Chem. Soc. Rev.* 2006, 35, 1162–1194.

[8] Walter M, Akola J, Lopez-Acevedo O, Jadzinsky PD, Calero G, Ackerson CJ, Whetten RL, Grönbeck H, Häkkinen H. A unified view of ligand-protected gold clusters as superatom complexes. *Proc. Natl. Acad. Sci. USA* 2008, 105, 9157–9162.

[9] Pensa E, Cortés E, Corthey G, Carro P, Vericat C, Fonticelli MH, Benítez G, Rubert AA, Salvarezza RC. The chemistry of the sulfur-gold interface: in search of a unified model. *Acc. Chem. Res.* 2012, 45, 1183–1192.

[10] Brust M, Walker M, Bethell D, Schiffrin DJ, Whyman R. Synthesis of thiol-derivatised gold nanoparticles in a two-phase liquid-liquid system. *J. Chem. Soc. Chem. Commun.* 1994, 801–802.

[11] Chaki NK, Negishi Y, Tsunoyama H, Shichibu Y, Tsukuda T. Ubiquitous 8 and 29 kDa gold:alkanethiolate cluster compounds: mass-spectrometric determination of molecular formulas and structural implications. *J. Am. Chem. Soc.* 2008, 130, 8608–8610.

[12] Wu Z, Jin R. On the ligand's role in the fluorescence of gold nanoclusters. *Nano Lett.* 2010, 10, 2568–2573.

[13] Zheng J, Petty JT, Dickson RM. High quantum yield blue emission from water-soluble Au8 nanodots. *J. Am. Chem. Soc.* 2003, 125, 7780–7781.

[14] Xie J, Zheng Y, Ying JY. Protein-directed synthesis of highly fluorescent gold nanoclusters. *J. Am. Chem. Soc.* 2009, 131, 888–889.

[15] Li G, Jin R. Atomically precise gold nanoclusters as new model catalysts. *Acc. Chem. Res.* 2013, 46, 1749–1758.

[16] Lin CJ, Yang T, Lee C, Huang SH, Sperling RA, Zanella M, Li JK, Shen J-L, Wang H-H, Yeh H-I, Parak WJ, Chang WH. Bioconjugation of fluorescent gold nanoclusters toward biological labeling. *ACS Nano* 2009, 3, 395–401.

[17] Häkkinen H. The gold–sulfur interface at the nanoscale. *Nat. Chem.* 2012, 4, 443–455.

[18] Negishi Y, Nobusada K, Tsukuda T. Glutathione-protected gold clusters revisited: bridging the gap between gold(I)-thiolate complexes and thiolate-protected gold nanocrystals. *J. Am. Chem. Soc.* 2005, 127, 5262–5270.

[19] Jadzinsky PD, Calero G, Ackerson CJ, Bushnell DA, Kornberg RD. Structure of a thiol monolayer-protected gold nanoparticle at 1.1 Å resolution. *Science* 2007, 318, 430–433.

[20] Jiang D. The expanding universe of thiolated gold nanoclusters and beyond. *Nanoscale* 2013, 5, 7149–7160.

[21] Qian H, Eckenhoff WT, Zhu Y, Pintauer T, Jin R. Total structure determination of thiolate-protected Au_{38} nanoparticles. *J. Am. Chem. Soc.* 2010, 132, 8280–8281.

[22] Zhu M, Aikens CM, Hollander FJ, Schatz GC, Jin R. Correlating the crystal structure of a thiol-protected Au_{25} cluster and optical properties. *J. Am. Chem. Soc.* 2008, 130, 5883–5885.

[23] Heaven MW, Dass A, White PS, Holt KM, Murray RW. Crystal structure of the gold nanoparticle $[N(C_8H_{17})_4][Au_{25}(SCH_2CH_2Ph)_{18}]$. *J. Am. Chem. Soc.* 2008, 130, 3754–3755.

[24] Zeng C, Qian H, Li T, Li G, Rosi NL, Yoon B, Barnett RN, Whetten RL, Landman U, Jin R. Total structure and electronic properties of the gold nanocrystal $Au_{36}(SR)_{24}$. *Angew. Chemie Int. Ed.* 2012, 51, 13114–13118.

[25] Crasto D, Malola S, Brosofsky G, Dass A, Häkkinen H. Single crystal XRD structure and theoretical analysis of the chiral $Au_{30}S(S\text{-}t\text{-}Bu)_{18}$ cluster. *J. Am. Chem. Soc.* 2014, 136, 5000–5005.

[26] Zeng C, Li T, Das A, Rosi NL, Jin R. Chiral structure of thiolate-protected 28-gold-atom nanocluster determined by X-ray crystallography. *J. Am. Chem. Soc.* 2013.

[27] Das A, Li T, Li G, Nobusada K, Zeng C, Rosi NL, Jin R. Crystal structure and electronic properties of a thiolate-protected Au_{24} nanocluster. *Nanoscale* 2014, 6, 6458–6462.

[28] Das A, Li T, Nobusada K, Zeng C, Rosi NL, Jin R. Nonsuperatomic $[Au_{23}(SC_6H_{11})_{16}]^-$ nanocluster featuring bipyramidal Au_{15} Kernel and Trimeric $Au_3(SR)_4$ Motif. *J. Am. Chem. Soc.* 2013, 135, 18264–18267.

[29] Das A, Liu C, Byun HY, Nobusada K, Zhao S, Rosi N, Jin R. Structure determination of $[Au_{18}(SR)_{14}]$. *Angew. Chem.* 2015, 127, 1–6.

[30] Chen S, Wang S, Zhong J, Song Y, Zhang J, Sheng H, Pei Y. The structure and optical properties of the $[Au_{18}(SR)_{14}]$ nanocluster. *Angew. Chemie Int. Ed.* 2015, 54, 1–6.

[31] Song Y, Wang S, Zhang J, Kang X, Chen S, Li P, Sheng H, Zhu M. Crystal structure of selenolate-protected $Au_{24}(SeR)_{20}$ nanocluster. *J. Am. Chem. Soc.* 2014, 24, 5–7.

[32] Song Y, Zhong J, Yang S, Wang S, Cao T, Zhang J, Li P, Hu D, Pei Y, Zhu M. Crystal structure of $Au_{25}(SePh)_{18}$ nanoclusters and insights into their electronic, optical and catalytic properties. *Nanoscale* 2014, 6, 13977–13985.

[33] Zeng C, Liu C, Chen Y, Rosi NL, Jin R. Gold-thiolate ring as a protecting motif in the $Au_{20}(SR)_{16}$ nanocluster and implications. *J. Am. Chem. Soc.* 2014, 20, 16–19.

[34] Zhang P. X-ray spectroscopy of gold–thiolate nanoclusters. *J. Phys. Chem. C* 2014, 118, 25291–25299.

[35] Rehr JJ, Albers RC. Theoretical approaches to x-ray absorption fine structure. *Rev. Mod. Phys.* 2000, 72, 621–654.

[36] Stern EA, Sayers DE, Lytle FW. Extended x-ray absorption fine-structure technique. III. Determination of physical parameters. *Phys. Rev. B* 1975, 11, 4836–4846.

[37] Menard LD, Xu H, Gao S-P, Twesten RD, Harper AS, Song Y, Wang G, Douglas AD, Yang JC, Frenkel AI, Murray RW, Nuzzo RG. Metal core bonding motifs of monodisperse icosahedral Au_{13} and larger Au monolayer-protected clusters as revealed by x-ray absorption spectroscopy and transmission electron microscopy. *J. Phys. Chem. B* 2006, 110, 14564–14573.

[38] Ankudinov AL, Ravel B, Rehr JJ, Conradson SD. Real-space multiple-scattering calculation and interpretation of x-ray-absorption near-edge structure. *Phys. Rev. B* 1998, 58, 7565–7576.

[39] Koningsberger DC, Mojet BL, Van Dorssen GE, Ramaker DE. XAFS spectroscopy; Fundamental principles and data analysis. *Top. Catal.* 2000, 10, 143–155.

[40] Macdonald MA, Chevrier DM, Zhang P, Qian H, Jin R. The structure and bonding of Au$_{25}$(SR)$_{18}$ nanoclusters from EXAFS: The interplay of metallic and molecular behavior. *J. Phys. Chem. C* 2011, 115, 15282–15287.

[41] Chevrier DM, MacDonald MA, Chatt A, Zhang P, Wu Z, Jin R. Sensitivity of structural and electronic properties of gold-thiolate nanoclusters to the atomic composition: a comparative x-ray study of Au$_{19}$(SR)$_{13}$ and Au$_{25}$(SR)$_{18}$. *J. Phys. Chem. C* 2012, 116, 25137–25142.

[42] Frenkel AI, Yevick A, Cooper C, Vasic R. Modeling the structure and composition of nanoparticles by extended x-ray absorption fine-structure spectroscopy. *Annu. Rev. Anal. Chem.* 2011, 4, 23–39.

[43] Schmid G. Developments in transition-metal cluster chemistry – the way to large clusters. *Struct. Bond.* 1985, 62, 51–85.

[44] Cluskey PD, Newport RJ, Benfield RE, Gurman SJ, Schmid G. An EXAFS study of some gold and palladium cluster compounds. In *Atoms, Molecules and Clusters*; 1993; Vol. 11, pp. S8–S11.

[45] Fairbanks MC, Benfield RE, Newport RJ, Schmid G. An EXAFS study of the cluster molecule Au$_{55}$(PPh$_3$)$_{12}$Cl$_6$. *Solid State Commun.* 1990, 73, 431–436.

[46] Marcus MA, Andrews MP, Zegenhagen J, Laboratories TB, Hill M, Montano P. Structure and vibrations of chemically produced Au$_{55}$ clusters. *Phys. Rev. B* 1990, 42, 3312–3316.

[47] Zhu Y, Qian H, Jin R. Catalysis opportunities of atomically precise gold nanoclusters. *J. Mater. Chem.* 2011, 21, 6793–6799.

[48] Yamazoe S, Koyasu K, Tsukuda T. Nonscalable oxidation catalysis of gold clusters. *Acc. Chem. Res.* 2013, 47, 816–824.

[49] Duchesne PN, Chen G, Zhao X, Zheng N, Zhang P. Surface reconstruction and reactivity of platinum–iron oxide nanoparticles. *J. Phys. Chem. C* 2014, 118, 28861–28867.

[50] Newton MA, Belver-Coldeira C, Martínez-Arias A, Fernández-García M. Dynamic in situ observation of rapid size and shape change of supported Pd nanoparticles during CO/NO cycling. *Nat. Mater.* 2007, 6, 528–532.

[51] Shivhare A, Chevrier DM, Purves RW, Scott RWJ. Following the thermal activation of Au$_{25}$(SR)$_{18}$ clusters for catalysis by x-ray absorption spectroscopy. *J. Phys. Chem. C* 2013, 117, 20007–20016.

[52] Liu J, Krishna KS, Losovyj YB, Chattopadhyay S, Lozova N, Miller JT, Spivey JJ, Kumar CSSR. Ligand-stabilized and atomically precise gold nanocluster catalysis: a case study for correlating fundamental electronic properties with catalysis. *Chem. Eur. J.* 2013, 19, 10201–10208.

[53] Stellwagen D, Weber A, Bovenkamp GL, Jin R, Bitter JH, Kumar CSSR. Ligand control in thiol stabilized Au$_{38}$ clusters. *RSC Adv.* 2012, 2, 2276–2283.

[54] Glaser T, Hedman B, Hodgson KO, Solomon EI. Ligand K-edge x-ray absorption spectroscopy: a direct probe of ligand-metal covalency. *Acc. Chem. Res.* 2000, 33, 859–868.

[55] MacDonald MA, Zhang P, Qian H, Jin R. Site-specific and size-dependent bonding of compositionally precise gold–thiolate nanoparticles from x-ray spectroscopy. *J. Phys. Chem. Lett.* 2010, 1, 1821–1825.

[56] Nishigaki J, Tsunoyama R, Tsunoyama H, Ichikuni N, Yamazoe S, Negishi Y, Ito M, Matsuo T, Tamao K, Tsukuda T. A new binding motif of sterically demanding thiolates on a gold cluster. *J. Am. Chem. Soc.* 2012, 134, 14295–14297.

[57] Yu Y, Luo Z, Chevrier DM, Leong DT, Zhang P, Jiang D, Xie, J. Identification of a highly luminescent Au$_{22}$(SG)$_{18}$ nanocluster. *J. Am. Chem. Soc.* 2014, 136, 1246–1249.

[58] Luo Z, Yuan X, Yu Y, Zhang Q, Leong DT, Lee JY, Xie J. From aggregation-induced emission of Au(I)–thiolate complexes to ultrabright Au(0)@Au(I)–thiolate core–shell nanoclusters. *J. Am. Chem. Soc.* 2012, 134, 16662–16670.

[59] Chevrier DM, Chatt A, Zhang P, Zeng C, Jin R. Unique bonding properties of the Au$_{36}$(SR)$_{24}$ nanocluster with FCC-like core. *J. Phys. Chem. Lett.* 2013, 36, 3186–3191.

[60] Kau DR, Alfonso D, Matranga C, Qian H, Jin R. A quantum alloy: the ligand-protected Au$_{25\text{-}x}$Ag$_x$(SR)$_{18}$ cluster. *J. Phys. Chem. C* 2013, 117, 7914–7923.

[61] Kurashige W, Munakata K, Nobusada K, Negishi Y. Synthesis of stable Cu$_{(n)}$Au$_{(25\text{-}n)}$ nanoclusters (n = 1–9) using selenolate ligands. *Chem. Commun. (Camb).* 2013, 49, 5447–5449.

[62] Kumara C, Aikens CM, Dass A. X-ray crystal structure and theoretical analysis of Au$_{25\text{-}x}$Ag$_x$(SCH$_2$CH$_2$Ph)$_{18}^-$ alloy. *J. Phys. Chem. Lett.* 2014, 5, 461–466.

[63] Negishi Y, Kurashige W, Kobayashi Y, Yamazoe S, Kojima N, Seto M, Tsukuda T. Formation of a Pd@Au$_{12}$ superatomic core in Au$_{24}$Pd$_1$(SC$_{12}$H$_{25}$)$_{18}$ probed by ^{197}Au Mossbauer and Pd K-Edge EXAFS spectroscopy. *J. Phys. Chem. Lett.* 2013, 4, 3579–3583.

[64] Yamazoe S, Kurashige W, Nobusada K, Negishi Y, Tsukuda T. Preferential location of coinage metal dopants (M = Ag or Cu) in [Au$_{25\ x}$M$_x$(SC$_2$H$_4$Ph)$_{18}$]$^-$ (x<1) As determined by extended x-ray absorption fine structure and density functional theory calculations. *J. Phys. Chem. C* 2014, 118, 25284–25290.

[65] Christensen SL, Macdonald MA, Chatt A, Zhang P. Dopant location, local structure, and electronic properties of Au$_{24}$Pt(SR)$_{18}$ nanoclusters. *J. Phys. Chem. C* 2012, 116, 26932.

[66] Kurashige W, Yamaguchi M, Nobusada K, Negishi Y. Ligand-induced stability of gold nanoclusters: thiolate versus selenolate. *J. Phys. Chem. Lett.* 2012, 3, 2649–2652.

[67] Yee CK, Ulman A, Ruiz JD, Parikh A, White H, Rafailovich M. Alkyl selenide- and alkyl thiolate-functionalized gold nanoparticles: chain packing and bond nature. *Langmuir* 2003, 19, 9450–9458.

[68] Kurashige W, Yamazoe S, Kanehira K, Tsukuda T, Negishi Y. Selenolate-protected Au$_{38}$ nanoclusters: isolation and structural characterization. *J. Phys. Chem. Lett.* 2013, 4, 3181–3185.

[69] Chevrier DM, Meng X, Tang Q, Jiang D, Zhu M, Chatt A, Zhang P. Impact of the selenolate ligand on the bonding behavior of Au$_{25}$ nanoclusters. *J. Phys. Chem. C* 2014, 25, 21730–21737.

[70] Kurashige W, Yamazoe S, Yamaguchi M, Nishido K, Nobusada K, Tsukuda T, Negishi Y. Au$_{25}$ clusters containing unoxidized tellurolates in the ligand shell. *J. Phys. Chem. Lett.* 2014, 5, 2072–2076.

[71] Jiang Y, Huang Y, Cheng H, Liu Q, Xie Z, Yao T, Jiang Z, Huang Y, Bian Q, Pan G, Sun Z, Wei S. Solvent influence on the role of thiols in growth of thiols-capped Au nanocrystals. *J. Phys. Chem. C* 2014, 118, 714–719.

[72] Li Y, Cheng H, Yao T, Sun Z, Yan W, Jiang Y, Xie Y, Sun Y, Huang Y, Liu S, Zhang J, Xie Y, Hu T, Yang L, Wu Z, Wei S. Hexane-driven icosahedral to cuboctahedral structure transformation of gold nanoclusters. *J. Am. Chem. Soc.* 2012, 134, 17997–18003.
[73] Ohyama J, Teramura K, Higuchi Y, Shishido T, Hitomi Y, Kato K, Tanida H, Uruga T, Tanaka T. In situ observation of nucleation and growth process of gold nanoparticles by quick XAFS spectroscopy. *ChemPhysChem* 2011, 12, 127–131.
[74] Yao T, Sun Z, Li Y, Pan Z, Wei H, Xie Y, Nomura M, Niwa Y, Yan W, Wu Z, Jiang Y, Liu Q, Wei S. Insights into initial kinetic nucleation of gold nanocrystals. *J. Am. Chem. Soc.* 2010, 132, 7696–7701.
[75] Yancey DF, Chill ST, Zhang L, Frenkel AI, Henkelman G, Crooks RM. A theoretical and experimental examination of systematic ligand-induced disorder in Au dendrimer-encapsulated nanoparticles. *Chem. Sci.* 2013, 4, 2912–2921.
[76] Kim P-SG, Hu Y, Brandys M-C, Burchell TJ, Puddephatt RJ, Sham TK. X-ray-excited optical luminescence (XEOL) and x-ray absorption fine structures (XAFS) studies of gold(I) complexes with diphosphine and bipyridine ligands. *Inorg. Chem.* 2007, 46, 949–957.
[77] Van Bokhoven Ja, Louis C, Miller JT, Tromp M, Safonova OV, Glatzel P. Activation of oxygen on gold/alumina catalysts: in situ high-energy-resolution fluorescence and time-resolved x-ray spectroscopy. *Angew. Chemie-Int. Ed.* 2006, 45, 4651–4654.

Bionotes

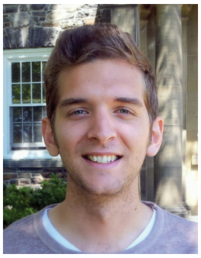

Daniel M. Chevrier
Department of Chemistry, Dalhousie University, Halifax, NS, Canada B3H 4R2

Daniel M. Chevrier completed a BSc Honors in Chemistry at Dalhousie University in 2011. He is currently a PhD student in the Chemistry Department at Dalhousie University under the supervision of Dr Peng Zhang and Dr Amares Chatt. His PhD research focuses on the X-ray spectroscopy characterization of atomically precise gold nanoclusters and luminescent protein-protected gold nanoclusters.

Rui Yang
Department of Chemistry, Dalhousie University, Halifax, NS, Canada B3H 4R2

Rui Yang received his BSc in Chemistry at St. Francis Xavier University in 2014, and he is currently a MSc student at Dalhousie University under the supervision of Dr Peng Zhang. His research interests focus on X-ray spectroscopy studies on thiolate-protected gold nanoclusters.

Amares Chatt
Department of Chemistry, Dalhousie University, Halifax, NS, Canada B3H 4R2

Amares Chatt received his BSc in 1964 from the University of Calcutta, India, his first MSc in 1967 from the University of Rookee, India, his second MSc in 1970 from the University of Waterloo, Canada and his PhD in 1974 from the University of Toronto, Canada. He has been a full Professor (1985–2008), Killam Professor of Chemistry (2001–2006), director of the SLOWPOKE-2 reactor facility (1987–2011), and is currently an Adjunct Professor of the Department of Chemistry, Dalhousie University in Halifax, Nova Scotia, Canada. His research interests include studies on X-ray spectroscopy of nanomaterials and γ-ray spectroscopy of radionuclides.

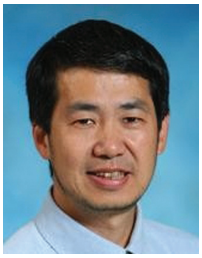

Peng Zhang
Department of Chemistry, Dalhousie University, Halifax, NS, Canada B3H 4R2; and School of Biomedical Engineering, Dalhousie University, Halifax, NS, Canada B3H 4R2
peng.zhang@dal.ca

Peng Zhang received his BSc (1993) and MSc (1997) from Jilin University and his PhD (2003) from the University of Western Ontario. He was an NSERC postdoctoral fellow at McGill University from 2003 to 2005. Currently, he is an Associate Professor in the Department of Chemistry, Dalhousie University in Halifax, Nova Scotia, Canada. His research focuses on the X-ray spectroscopy studies of nanomaterials and their applications in catalysis and biomedicine.